Optimizing Interface Conductivity in Electronics

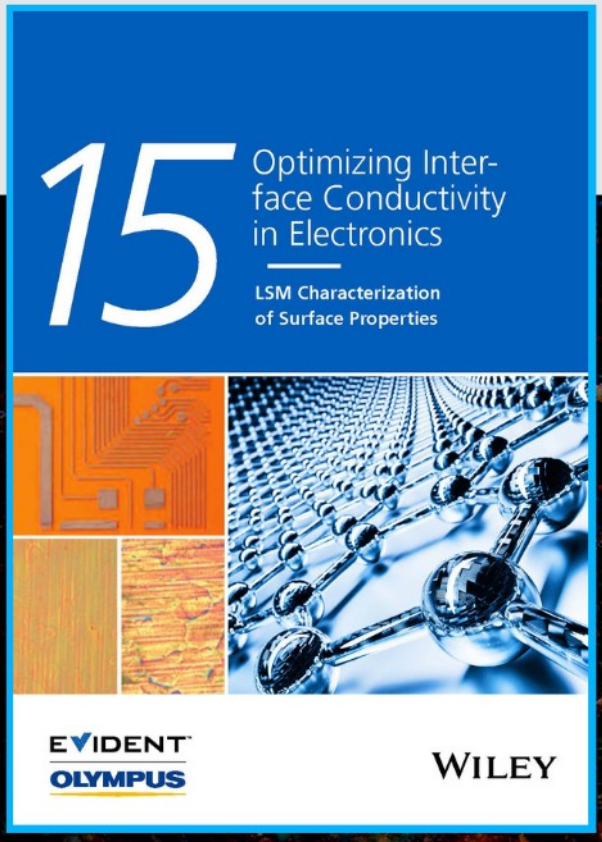

The latest eBook from Advanced Optical Metrology. Download for free.

Surface roughness is a key parameter for judging the performance of a given material's surface quality for its electronic application. A powerful tool to measure surface roughness is 3D laser scanning confocal microscopy (LSM), which will allow you to assess roughness and compare production and finishing methods, and improve these methods based on mathematical models.

Focus on creating high-conductivity electronic devices with minimal power loss using laser scanning microscopy is an effective tool to discern a variety of roughness parameters.

EVIDENT
OLYMPUS

WILEY

ADVANCED FUNCTIONAL MATERIALS
www.afm-journal.de

Hybrid Organic–Inorganic Halide Post-Perovskite 3-Cyanopyridinium Lead Tribromide for Optoelectronic Applications

Nikita I. Selivanov, Anna Yu. Samsonova, Ruslan Kevorkyants, Irina V. Krauklis, Yuri V. Chizhov, Boris V. Stroganov, Marios E. Triantafyllou-Rundell, Detlef W. Bahnemann, Constantinos C. Stoumpos, Alexei V. Emeline, and Yury V. Kapitonov*

2D halide perovskite-like semiconductors are attractive materials for various optoelectronic applications, from photovoltaics to lasing. To date, the most studied families of such low-dimensional halide perovskite-like compounds are Ruddlesden–Popper, Dion–Jacobson, and other phases that can be derived from 3D halide perovskites by slicing along different crystallographic directions, which leads to the spatially isotropic corner-sharing connectivity type of metal-halide octahedra in the 2D layer plane. In this work, a new family of hybrid organic–inorganic 2D lead halides is introduced, by reporting the first example of the hybrid organic–inorganic post-perovskite 3-cyanopyridinium lead tribromide (3cp)$PbBr_3$. The post-perovskite structure has unique octahedra connectivity type in the layer plane: a typical "perovskite-like" corner-sharing connectivity pattern in one direction, and the rare edge-sharing connectivity pattern in the other. Such connectivity leads to significant anisotropy in the material properties within the inorganic layer plane. Moreover, the dense organic cation packing results in the formation of 1D fully organic bands in the electronic structure, offering the prospects of the involvement of the organic subsystem into material's optoelectronic properties. The (3cp)$PbBr_3$ clearly shows the 2D quantum size effect with a bandgap around 3.2 eV and typical broadband self-trapped excitonic photoluminescence at temperatures below 200 K.

1. Introduction

Halide perovskites, known and studied[1–3] for more than a century, attracted attention in the mid-2010s due to the possibility of their use for the absorber layer in solar cells.[4] In parallel with the record achievements in the efficiency of perovskite solar cells,[5] the possibilities of using these unique semiconductors in other fields of optoelectronics, such as photodetectors,[6] light-emitting diodes,[7] lasers active media,[8] γ- and X-ray detectors,[9] to name a few, are opening up. The structural formula of halide perovskite crystals is ABX_3, where B^{2+} is a metal cation (usually Pb^{2+} or Sn^{2+}), X^- is a halide anion (I^-, Br^-, or Cl^-), and A^+ is either an inorganic or an organic cation in fully inorganic and hybrid organic–inorganic halide perovskites, respectively. The main building blocks of the 3D perovskite inorganic frameworks are the $[BX_{6/2}]$ octahedra, connected in a corner-sharing manner along the three orthogonal spatial dimensions. Such infinite frameworks are only stable when the A cations have suitable sizes limited by the Goldschmidt relation[10] for ionic solids.

Violation of this limitation could lead to edge- or face-sharing octahedra connectivity or leave some of X^- anions as terminal ligands. This structural versatility results in a huge variety of perovskite-like structures of ABX_3 or dimensionally reduced stoichiometries. Some B—X framework types could be obtained in fully inorganic

Dr. N. I. Selivanov, A. Y. Samsonova, Dr. R. Kevorkyants, Dr. I. V. Krauklis, Prof. Y. V. Chizhov, B. V. Stroganov, Prof. D. W. Bahnemann, Prof. A. V. Emeline, Dr. Y. V. Kapitonov
Physics faculty
Saint Petersburg State University
7/9 Universitetskaya Emb., St. Petersburg 199034, Russia
E-mail: bahnemann@iftc.uni-hannover.de

The ORCID identification number(s) for the author(s) of this article can be found under https://doi.org/10.1002/adfm.202102338.

DOI: 10.1002/adfm.202102338

M. E. Triantafyllou-Rundell, C. C. Stoumpos
Department of Materials Science and Technology
Voutes Campus
University of Crete
Heraklion 70013, Greece

Prof. D. W. Bahnemann
Institut fuer Technische Chemie
Gottfried Wilhelm Leibniz Universitaet Hannover
Callinstrasse 3, Hannover D-30167, Germany

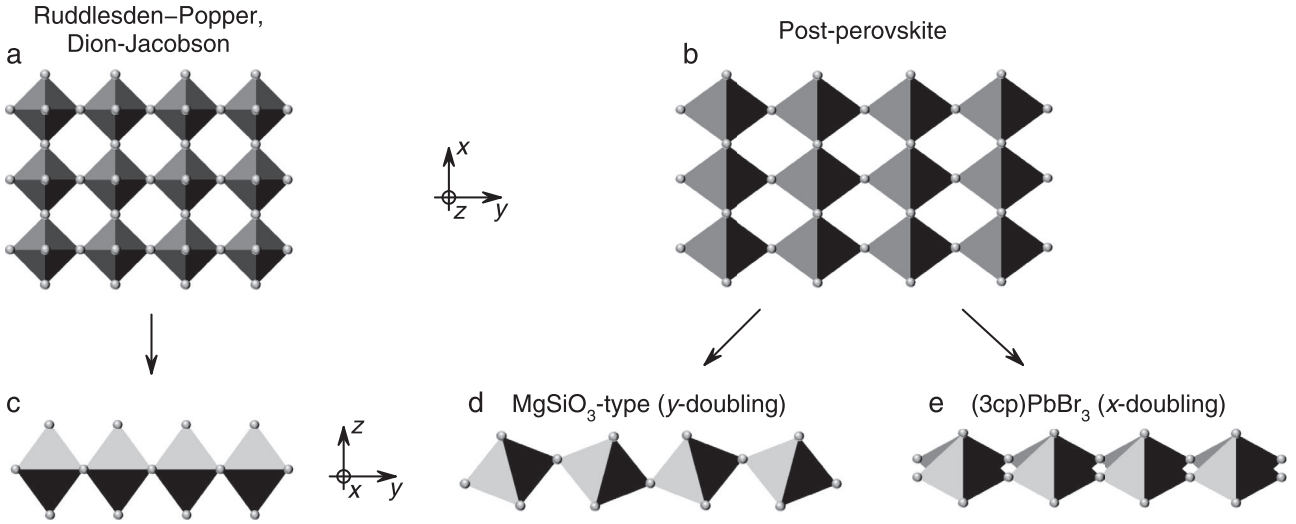

Figure 1. Schematic crystal structures of connected [BX_6] octahedra frameworks for Ruddlesden–Popper and Dion–Jacobson phases (a,c), and for post-perovskite phase (b,d,e) viewed along the stacking *z*-axis (a,b) and in-plane *x*-axis (c,d,e). Symmetry lowering in actual post-perovskite structures by doubling the lattice constant along the *y*-axis in $MgSiO_3$-type and *x*-axis in (3cp)$PbBr_3$ crystal types are shown.

perovskite-like compounds,[11,12] but the greatest variety can be achieved via the organic A cations' substitution. Low-dimensional perovskite-like structures are of particular practical interest, among which quasi-2D crystals got the most attention.[13,14] The 2D perovskite-like semiconductors are natural multiple quantum wells (QWs) with well-pronounced quantum size effect, increased exciton binding energy and oscillator strength,[15,16] and are praised for their stability[17] and possibility of being used in various optoelectronic applications, ranging from photovoltaics[18] to lasers.[19]

The broadest order of hybrid organic–inorganic quasi-2D perovskite-like structures[20] could be imagined by slicing off layers from ABX_3 perovskites framework along the (100), (110), or (111) directions with organic cations serving as spacers. The (100)-oriented cleaves lead to the mostly studied Ruddlesden–Popper (RP) and Dion–Jacobson (DJ) families.[13] **Figure 1**a,c shows inorganic layers of these two homologous families for $n = 1$. Therein, the corner-sharing octahedral connectivity in the layer plane inherited from the 3D-perovskite ancestor results in the material isotropy in *x*- and *y*-directions.

Despite the tremendous possibilities of controlling the crystal structure by selecting the organic cations, not all the possible analogous structures found in oxide perovskite derivatives have been realized in their halide counterparts.

One of the most unexpected oxide perovskite-like crystal structures comes from geophysics. Seismic observation of the Earth's interior led to the discovery of unexpected features of the lowermost mantle region called the D″ layer. Most of the lower mantle is composed of $MgSiO_3$ perovskite. It was expected that in the D″ layer this mineral undergoes phase transition, and new phase would explain abnormal properties of this layer. In 2004 this question was resolved by the discovery of $MgSiO_3$ polytype[21,22] named "post-perovskite." $MgSiO_3$ post-perovskite exists at a pressure of >125 GPa and a temperature of 2500 K. This phase consists of $[SiO_{6/2}]^{2-}$ octahedra, forming layers with corner- and edge-sharing connectivity in orthogonal directions across the layers' plane separated by Mg^{2+} cations between the layers. This connectivity is schematically shown in Figure 1b. The post-perovskite structure is quite uncommon, and it is only known in the $MgGeO_3$,[23] $MnGeO_3$,[24] $CaIrO_3$,[25] $CaRuO_3$,[26] and $CaPtO_3$[27] among oxides. Other material families that host the post-perovskite structure include the $NaMgF_3$[28] fluoride, and the β-$LnLuSe_3$ (Ln = Pr and Nd)[29] and $UFeE_3$ (E = S and Se)[30] chalcogenides. The structure of Cr_3GeC is an example of the anti-post-perovskite structure in carbide chemistry.[31] The only known heavy halide post-perovskite is fully inorganic $TlPbI_3$.[11,32] Despite its toxicity, this material already attracted attention for possible ionizing radiation detection.[33] It should be noted that in all the post-perovskites mentioned above the crystal structures adopt the based-centered orthorhombic *Cmcm* space group containing two layers of corrugated octahedra sheets within the unit cell as shown in Figure 1d. This structure could be represented as a high-symmetry structure (Figure 1b) with the lattice constant doubling along the *y*-direction due to the octahedra tilts. For hybrid organic–inorganic lead halides, only 1D chains with post-perovskite connectivity types were synthesized so far.[34]

In this work, we introduce a new family of hybrid organic–inorganic 2D lead halides by reporting the first example of the hybrid organic–inorganic post-perovskite (3cp)$PbBr_3$,where 3cp stands for the 3-cyanopyridinium, $[3\text{-}CN{-}C_5H_5NH]^+$, cation. We experimentally explore its structural, optical, and vibrational properties, and predict its electronic structural peculiarities by theoretical calculations. The different octahedra's connectivities across the inorganic framework layers give rise to the material anisotropy, while the dense organic cations' packing offers prospects of the involvement of the organic subsystem into material's optoelectronic properties.

2. Results and Discussion

2.1. Crystal Growth and Characterization

Centimeter-sized (3cp)$PbBr_3$ single crystals were grown by the slow counterdiffusion of individual solutions of lead(II) bromide ($PbBr_2$) and 3-cyanopyridine in HBr in the silica gel filled

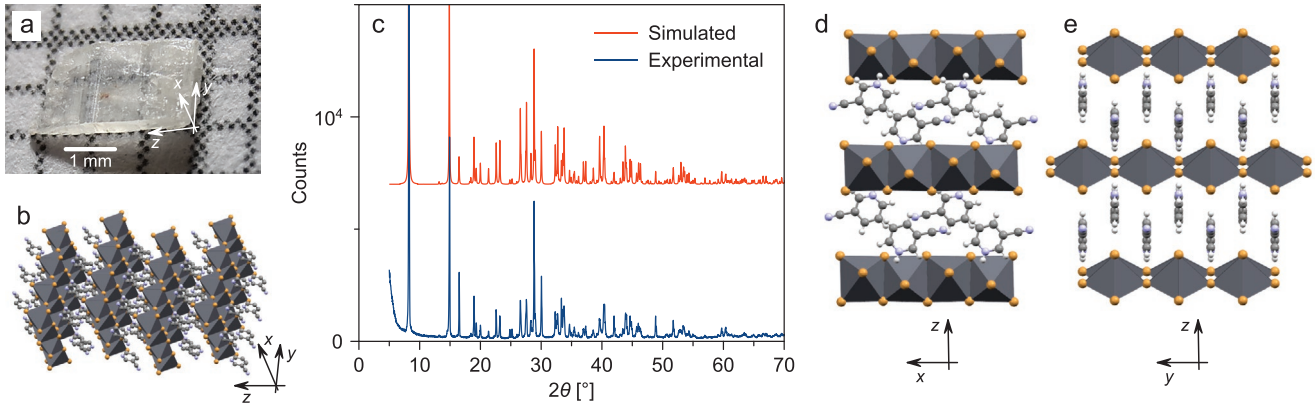

Figure 2. The a) photo and b) the structure of (3cp)$PbBr_3$ crystal. [$PbBr_6$] octahedra are shown in gray. Hydrogen atoms are omitted for clarity. c) XRD patterns for powdered crystal (blue) and simulated patterns based on the single-crystal XRD data (red). Crystal structure seen along the d) *y*-axis and e) *x*-axis. Atom colors: Pb—gray, Br—orange, C—light gray, N—light blue, and H—white.

U-tube. This gel growth method has proved applicable for a synthesis of low-dimensional organic–inorganic lead halides[35] and 3D perovskites $MAPbX_3$ (X = I and Br)[36] of high crystal and optical quality. The as-grown (3cp)$PbBr_3$ crystal plates are optically translucent and have well-defined rectangular morphology (**Figure 2**a). The crystals are quite stable and retained their properties after 20 months of storage in a dry atmosphere.

2.2. Crystal Structure

Single crystal X-ray diffraction (XRD) study of (3cp)$PbBr_3$ at 300 K revealed its post-perovskite-type structure (Figure 2b; Figure S1b and Table S2, Supporting Information) with *C*2/*m* monoclinic space group with (*x*, *y*, *z*) axes in Figure 1 roughly corresponding to (*c*, *b*, *a*) lattice vectors. The single-phase formation during the synthesis was confirmed by powder XRD analysis of the grinded single crystals (Figure 2c). Note that, unlike $MgSiO_3$-type post-perovskites (Figure 1d), the crystal structure of (3cp)$PbBr_3$ exhibits the lattice constant doubling along the *x*-axis, caused by the distortion of the [BX_6] octahedra in addition to the regular distortion of the structure type (Figure 1e). This distortion is responsible for the lowering of the symmetry from orthorhombic *Cmcm* (parent) to the monoclinic *C*2/*m* (child) space group. Unlike RP and DJ structures (Figure 1a), the distribution of octahedra in (3cp)$PbBr_3$ is not uniform in the (*x*,*y*) plane, arranging in "ridges" of edge-shared anions and "grooves" of corner-shared ones along the *x*-axis (Figure 2d). Such anisotropy results in perfect ordering of 3-cyanopyridinium cations along the *x*-axis in the "grooves" with the pyridinium nitrogen atoms being anchored inside the grooves (Figure 2e). The formation of "ribs" in "grooves" is caused by deformation of the [BX_6] octahedra, confining the placement of the organic cations along the *x*-axis. This leads to the doubling of the lattice constant along the *x*-axis. In this configuration, the Pb^{2+} cations are shifted from the octahedra centers (Figure S5, Supporting Information).

The crystal packing of the 3-cyanopyridinium cations in (3cp)$PbBr_3$ crystal allows for short interatomic distances between pyridinium nitrogen atom and bromides (distances are shown in Figure 5e,f). The shortest N···Br distance equal to 3.28 Å allows us to make an assumption about the presence of a hydrogen bond between the corresponding hydrogen and bromine atoms (Figure 5f).[37] These bonds together with the π–π stacking interactions discussed in the following sections likely serve as the stabilizing forces for the orientation and mutual arrangement of 3-cyanopyridinium cations in the organic layer.

Refinement of the XRD data at 100 K (Table S2, Supporting Information) reveals a lower-symmetry unit cell for (3cp)$PbBr_3$, crystallizing in the triclinic *P*-1 space group (Figure S1a, Supporting Information). The phases can be transformed into one another via a phase transition, occurring between 300 and 100 K.

To determine the orientation of the as-grown single crystals, electron backscatter diffraction (EBSD) and powder XRD of single crystals were used. **Figure 3**a shows the EBSD pattern obtained for the crystal. This pattern could be perfectly fit using the known crystal structure (Figure 3b) with the orientation being depicted for the crystal in Figure 2a. Surprisingly, the direction of the inorganic framework planes is orthogonal to crystal plate. This indicates a slower crystal growth along the *x*-axis, i.e., the edge-sharing direction. An additional confirmation

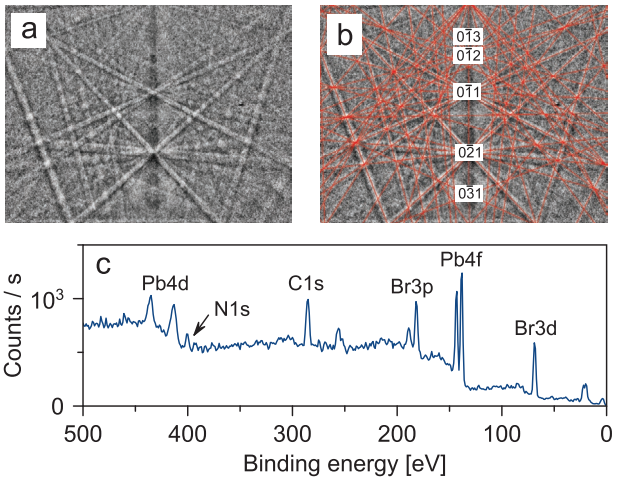

Figure 3. a) EBSD pattern of (3cp)$PbBr_3$ single crystal and b) its solution using known crystal structure. c) XPS spectra of (3cp)$PbBr_3$ with peaks attribution.

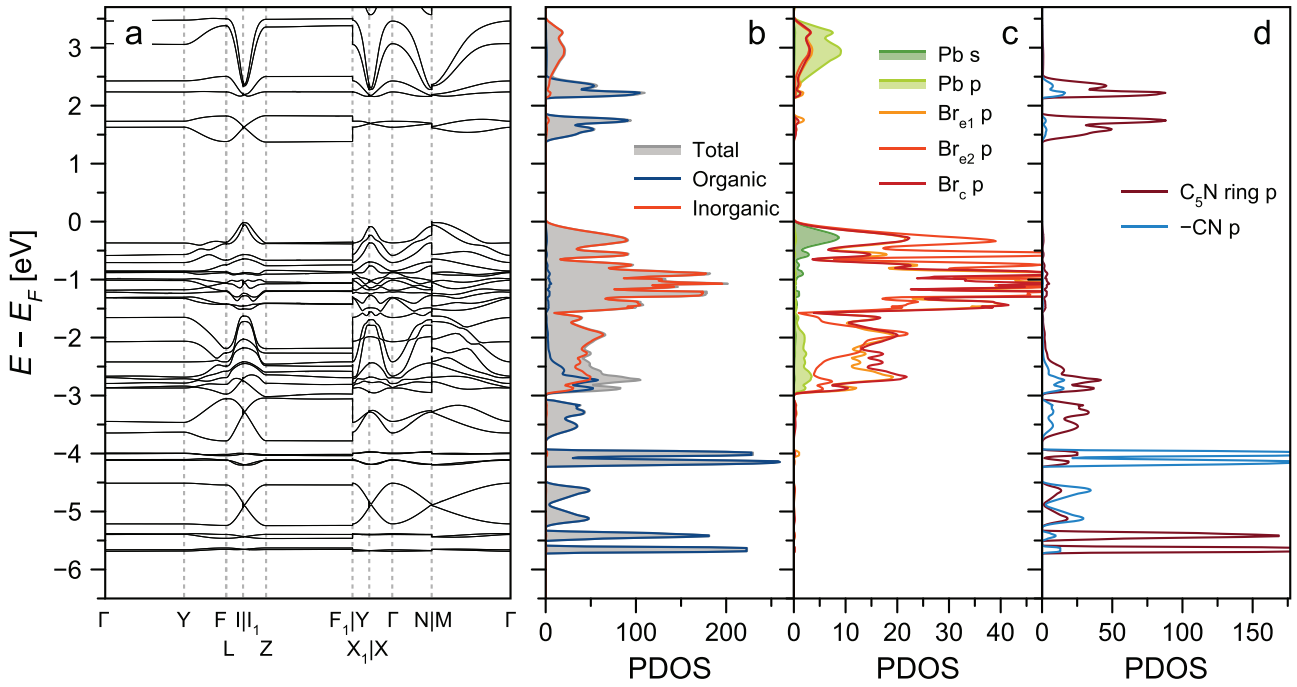

Figure 4. Calculated electronic structure of (3cp)$PbBr_3$: a) band structure, b) total density of states (DOS) and organic/inorganic subsystems contribution, and DOS of c) inorganic and d) organic subsystems.

of the chosen orientation is the observation of (002) and (004) reflections in the XRD scan of the single crystal in the orientation shown in Figure S6 (Supporting Information). (3cp)$PbBr_3$ single crystals have cleavage planes along (*xz*) and (*xy*) planes (Figure S7, Supporting Information), indicating the ease of breaking corner-sharing bonds and weak bond between alternating organic and inorganic layers, respectively. Absence of cleavage along the (*yz*) plane could be explained by the bond strength of edge-sharing octahedra connectivity. Figure 3c shows the X-ray photoelectron spectrum (XPS) of the (3cp)$PbBr_3$ single crystal. Br3d and Pb4f signals (Figure S8, Supporting Information) confirm the expected oxidation states of bromide and lead atoms in the compound.

2.3. Electronic Structure

Density functional theory (DFT) modeling of (3cp)$PbBr_3$ was performed with the crystal structure obtained at 300 K with spin–orbit coupling effects being included. Calculated electronic band structure and density of states (DOS) are shown in **Figure 4**.

As can be seen from Figure 4c, the compounds' valence band consists of p-orbitals of Br and s-orbitals of Pb, which is typical of lead halides.[38] The unoccupied inorganic bands consisting of p-orbitals of Pb and Br are observed at >2.4 eV. Additionally, two organic-related bands are observed between the abovementioned inorganic bands. Appearance of similar organic-related bands was already reported for pyridinium and 3-hydroxypyridinium cations in lead trihalides.[39] However, the reported bands were flat, which indicated the localization of electron density predominantly on the organic cations weakly interacting with each other and with an inorganic subsystem. In our case, the tight packing of cyanopyridinium cations, their zig-zag stacking orientation within the interlayer space, and increase in the size of their molecular π-orbitals due to the −C≡N group led to the onset of the weak bonding interaction between cations, and the formation of the dispersive bands, observed in the calculations. In attempt to deconvolute these bands, we performed calculations starting with single 3-cyanopyridinium cations.

The 3-cyanopyridinium cation is isoelectronic to 3-cyanopyridine because it is formed by the addition of a proton. To better understand the electronic structure, 3-cyanopyridine can be roughly represented as a combination of pyridine and −CN group from hydrogen cyanide. Figure S9 (Supporting Information) shows the π-molecular orbitals and the corresponding eigenenergies for 3-cyanopyridine 3-CN−C_5H_4N, and its constituent analogs (benzene (C_6H_6), pyridine (C_5H_5N), and hydrogen cyanide (HCN)) calculated by the DFT method wB97X/6–311G(d,p). The full set of calculated parameters for highest molecular orbitals could be found in Table S10 (Supporting Information).

In the benzene molecule, the lowest unoccupied molecular orbitals (LUMO) are degenerated π_4* and π_5* antibonding π-molecular orbitals. In the isoelectronic pyridine, this degeneracy is removed due to the symmetry breaking of the ring upon substitution of one of the carbon atoms with a nitrogen atom leading to the splitting of the corresponding molecular orbitals.

On the other hand, the LUMO of hydrogen cyanide consists of degenerate π_3* and π_4* antibonding π-molecular orbitals. With this combination, only the −CN group π-orbital orthogonal to the pyridine ring plane can interact with the pyridine π-system. This leads to the formation of two unoccupied π-conjugated molecular orbitals π_5* and π_6* due to the bonding interaction of π_4* and π_5* orbitals of pyridine with π_4* of the −CN group. The π_5* and π_6* orbitals of 3-cyanopyridine are

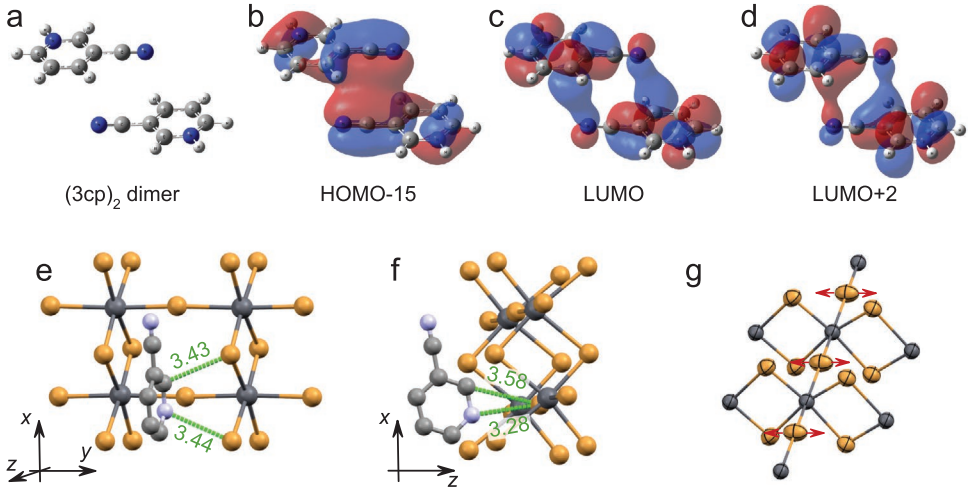

Figure 5. a) Cation dimer arrangement and b–d) its molecular orbitals demonstrating the stacking interaction. e,f) Fragments of the crystal structure with shortest distances between organic and inorganic atoms shown in Å. Atoms colors: Pb—gray, Br—orange, C—light gray, and N—light blue. Hydrogen atoms are omitted for clarity. g) Thermal ellipsoids for $T = 300$ K with 90% probability. Red arrows show excessive movement freedom of corner-shared Br atoms.

further split for 0.457 eV. Similar lineage could be drawn up for occupied π-conjugated 3-cyanopyridine orbitals π_1, π_2, π_3, and π_4.

Next, we consider intermolecular interactions of the 3-cyanopyridinium dimer (Figure S9, Supporting Information) with cations' orientation and interatomic distances obtained from the room-temperature crystal structure. Although this calculation does not capture the electronic properties of the crystal and ignores the crystal field potential, it allows for a qualitative assessment of the intermolecular interactions. The mutual orientation of the cations and the small distance between them favor the stacking interaction between their π-conjugated systems. The shortest distance of 3.265 Å is observed between the nitrogen atom in the −CN group of one cation, and the carbon atom in the fourth (counting from the nitrogen atom in the pyridinium ring) position in the ring of the adjacent cation. Stacking interaction leads to the formation of bonding and antibonding combinations of 3-cyanopyridinium cation π-molecular orbitals with the splitting between their energies being the measure of the interaction strength (Figure 4b).

The maximum splitting of 0.45 eV is for the occupied $\pi_2 \pm \pi_2$ orbitals' interaction (Table S12, Supporting Information), and 0.241 and 0.101 eV splitting for $\pi_5^* \pm \pi_5^*$ and $\pi_6^* \pm \pi_6^*$ unoccupied orbitals' interactions, respectively. **Figure 5**a–d shows several molecular orbitals with electron density in the shortest intermolecular distance direction being clearly visible. According to calculations, the differences in total energy in the formation of a stacking dimer from 3-cyanopyridinium cations are –6.65 and –7.41 kcal mol^{-1} with dispersion interactions being taken into account.

This calculation was performed for a dimer, while the transition to an infinite crystal will lead to the formation of bands with electron density being delocalized by stacking interactions in the y-direction. The shortest distance of 3.515 Å between carbons in fifth positions in the rings of cations in adjacent chains prevents the further delocalization in the x-direction, so 1D organic bands are formed. Thus, organic bands at 1.4–1.8 and 2.1–2.5 eV were identified as delocalized $\pi_5^* \pm \pi_5^*$ and $\pi_6^* \pm \pi_6^*$ molecular orbitals of 3-cyanopyridinium cations. Similar bands formed by occupied orbitals are of less interest, since they are located deep in the valence band of (3cp)$PbBr_3$.

Presence of weak hydrogen bonds also leads to the insignificant admixture of bands despite this, which can still be classified as organic and inorganic in origin (Figure 4b). Little spatial overlap of inorganic and organic bands (e.g., based on partial DOS in Figure 4b) leads to the negligible transition dipole moment between the inorganic states at valence band maximum and unoccupied organic states. Thus, such transitions do not participate in the absorption of light, and bandgap should be estimated only by consideration of the inorganic bands. In this case, the valence band maximum is located at nearly equivalent I, I_1, N, and M points, and the conduction band minimum in X-point, thus, leading to the indirect transition with the calculated bandgap of 2.27 eV (Figure S13, Supporting Information). It should be noted that the calculation shows only 0.01 eV higher energy for the minimum at M-point, which leaves the possibility of the direct transition in this material in fact. Since unoccupied organic bands are lying in the bandgap, they could act as deep defect states analogous to Bi-doped halide perovskites.[40,41]

2.4. Optical Spectroscopy

Diffuse reflectance spectra (DRS) of the grounded (3cp)$PbBr_3$ crystal were used for the determination of the absorption edge. **Figure 6**a shows the room-temperature Kubelka–Munk function $F(R) = (1 - R)^2/2R$, where R is the measured diffuse reflectance coefficient. The derivative dF/dE in Figure S14 (Supporting Information) shows the maximum at 3.25 eV correlated to the fundamental absorption at the material band edge.

The photoluminescence (PL) spectrum at $T = 77$ K with excitation well above the absorption edge ($E_{ex} = 3.31$ eV) shows a broad emission peak centered at $E_{em} = 2.45$ eV (Figure 6b). The emission peak's full width at half maximum (FWHM) is 0.36 eV. Such broad emission probably derives from the self-trapped exciton (STE) recombination, a well-known phenomenon in

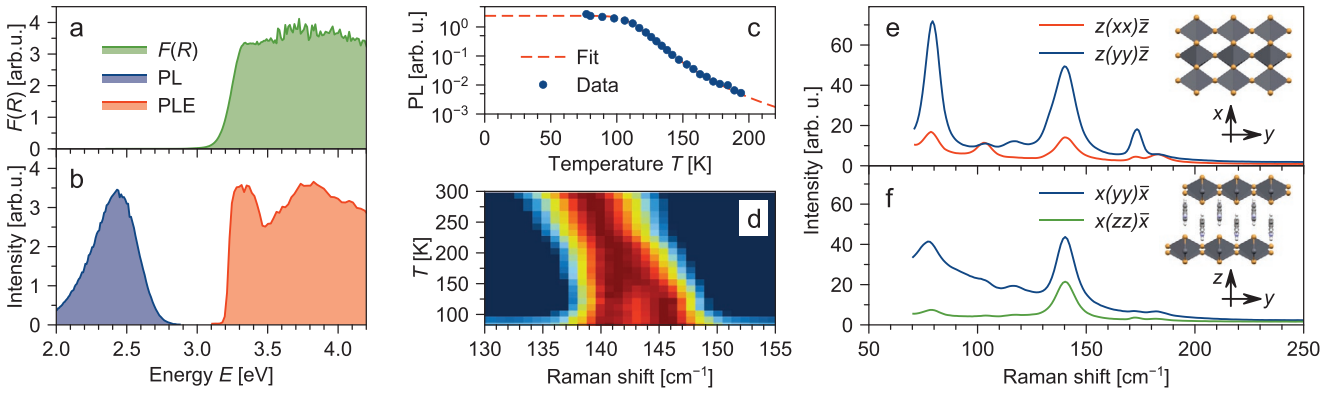

Figure 6. a) Kubelka–Munk function $F(R)$ at $T = 300$ K. b) PL ($E_{ex} = 3.31$ eV) and PLE ($E_{em} = 2.45$ eV) spectra at $T = 77$ K. c) PL temperature dependence (dots) and Arrhenius fit (dashed line). d) Normalized unpolarized Raman scattering temperature dependency. e,f) Polarized Raman scattering at $T = 300$ K. Insets show crystal orientation. Porto notation is used for polarized scattering geometry.

low-dimensional lead halides.[42] Photoluminescence excitation (PLE) measurements at E_{em} show sharp edge at 3.18 eV, which is consistent with the bandgap determined by the DRS measurements (Figure 6b). This value is larger than the bandgap calculated by DFT (2.34 eV for the direct transition between inorganic bands) due to the well-known tendency of DFT calculations to underestimate the energy bandgap.

The studied 2D lead bromide's band edge is blueshifted by 0.9 eV in comparison with the 3D $MAPbBr_3$ perovskite band edge.[43] This is a manifestation of the quantum size effect in natural multiple QWs formed by inorganic framework layers of $(3cp)PbBr_3$. This also confirms the fact that despite the slight interaction of organic and inorganic subsystems described above, there are no charge-transfer signatures through the organic layer. Thus, we conclude that the organic layer acts as a QW barrier. The redshift of 0.4 eV between the absorption edge and PL emission maximum is a sum of exciton binding energy and STE trapping energy. Absence of the free exciton emission feature (not observed in PL down to $T = 4$ K) prevents separation of these two contributions. As the temperature rises, PL emission gradually disappears without significant spectral shift or broadening (Figure S15, Supporting Information). PLE edge also remains unshifted (Figure S15, Supporting Information). The temperature dependency of the PL emission intensity was fitted by the Arrhenius equation $I = I_0/(1 + A\exp(-E_a/k_BT))$, yielding the activation energy E_a of the PL quenching processes of 0.14 eV (Figure 6c).

2.5. Vibrational Spectroscopy

Different connectivities of octahedra in the inorganic layer of $(3cp)PbBr_3$ along x- and y-directions should lead to a significant anisotropy of electron–phonon interaction. In order to probe experimentally this anisotropy, polarized Raman spectra were measured at room temperature in different geometries (Figure 6e,f). Observed low-frequency signals (<200 cm^{-1}) correspond to vibrations of the inorganic framework. Figure 5e shows the larger amplitude of the co-polarized Raman signal for vibrations along the octahedra corner-sharing axis (y-axis) in comparison with vibrations along the edge-sharing axis (x-axis) for excitation normal to the inorganic layers' plane. This effect is the manifestation of the higher amplitude of vibrations of corner-shared Br atoms, which could also be seen in structural data by observation of thermal ellipsoids at 300 K (Figure 5g). Even a more pronounced effect could be seen for the excitation along the x-axis (Figure 6f). A similar effect of an increase in the amplitude and broadening of the Raman signal was observed for 3D halide perovskites in those cases when a motion freedom of the A cation exists in the crystal lattice.[44–47]

Raman spectroscopy was also used to reveal the phase transition between high-temperature $C2/m$ and low-temperature $P\text{-}1$ phases. The measured temperature dependence of the Raman signal for the region around 140 cm^{-1} is shown in Figure 6d. At 100 K, the signal is split into two lines (140 and 146 cm^{-1}). With the temperature growth, these two lines merge at a temperature of around 200 K, which is the manifestation of the crystal symmetry increase.

3. Conclusion

In this work, we have introduced the first member of a new family of 2D hybrid organic–inorganic halides, in the form of $(3cp)PbBr_3$ post-perovskite. The first member of this family—(3cp)PbBr3—was synthesized using the innovative gel growth method, and characterized both experimentally and theoretically. Optical measurement on single crystals of this material demonstrates a bandgap of 3.2 eV and a broadband self-trapped excitonic photoluminescence below 200 K. The material undergoes a structural phase transition at around 200 K, reducing its crystal lattice symmetry from monoclinic to triclinic. DFT calculations show that dense packing of organic cations leads to the formation of 1D fully organic band. However, this band does not directly participate in the optical response. Anisotropy of the post-perovskite structure in the layer plane manifests itself in the anisotropy of electron–phonon coupling pathways, evidenced by the different thermal motion of the corner- (perovskite-like) and edge-shared octahedra. Ongoing work is focused on finding other representatives of this family, studying the possibility of functionalizing the organic A-site cation and the development of routes toward practical application of

these materials in optoelectronics, for example, as white-light emitters or ionizing radiation detectors.

4. Experimental Section

Reagents: Lead(II) bromide (98%, Sigma–Aldrich), aqueous HBr (40%, Iodobrom), and 3-cyanopyridine (98%, Alfa Aesar) were used as received. Silica gel was prepared from sodium metasilicate crystallohydrate solution ($Na_2SiO_3 \cdot 9H_2O$) with the distilled water as solvent.

Crystal Growth: In the present work, the modification of the method used for a synthesis of 1D piperidinium lead triiodide in silicate gel[38] was employed. The method is based on a difference in solubility of a target perovskite and lead halide in corresponding hydrohalic acid.

Crystal Characterization: Single crystal X-ray diffraction study of the obtained single crystals was carried out using the diffractometer Agilent Technologies Xcalibur (Oxford Diffraction). The apparatus included an anode—MoKα X-ray tube and a detector of reflected X-rays—the high-speed position-sensitive CCD "Atlas." The structure was solved using charge flipping methods and it was subsequently refined using the Jana2006 software.[48,49] XRD measurements were performed at two different temperatures of 100 and 300 K. Powder X-ray diffraction study was conducted using the Bruker D2 Phaser diffractometer from powdered single crystals and the high-resolution X-ray diffractometer Bruker D8 Discover using a long focus X-ray tube Cu Kα anode. Reflected X-rays were detected using a solid position-sensitive detector LYNXEYE.

The EBSD measurements were carried out using a backscattered electron diffraction detector, OxfordHKL NordLys Nano equipped on a Hitachi S-3400N scanning electron microscope. Due to the structure, photodegradation under electron beam EBSD images' acquisition was performed as follows: multiple images (50–100) from an area of 40 × 40 μm were collected (exposure: 50 ms per image) and averaged. Pattern indexing was performed using Oxford AzTec software using 300 K crystal structure as a model.

The XPS spectra were collected using Thermo Fisher Scientific ESCALAB 250Xi setup with the Al Kα X-ray source (1486.6 eV with a monochromator), variable beam size (200–900 mkm), and an energy resolution of 0.45 eV.

Electronic Structure Calculations: Electronic structure calculations of (3cp)$PbBr_3$ were performed within the framework of periodic DFT using Abinit-8.2.3 program.[50] Local density approximation density functional[51] was applied. Spin–orbit coupling was accounted for using relativistic separable Hartwigsen–Goedecker–Hutter pseudopotentials.[52] In both the band structure and projected density of state calculations, the Brillouin zone was sampled over 4 × 4 × 4 Γ-centered Monkhorst–Pack grid of *k*-points.[53] The applied kinetic energy cut-off was equal to 60 Hartree. The band structure was computed along the *Γ*–*Y*–*F*–*L*–*I*–*I1*–*Z*–*F1*–*Y*–*X1*–*X*–*Γ*–*N*–*M*–*Γ* path[54] of high-symmetry *k*-points of monoclinic reciprocal lattice.

The DFT calculations of molecular orbitals were performed with the long-range corrected wB97X/6–311G(d,p) functional, which was allowed for accurately estimating the ionization potentials of pyridines. In models of single and dimer organic cations, Br^- anions were added in calculation in order to neutralize the excessive positive charge. In optimization of the geometry, each of the N, Br, and C6 atoms of the 3-cyanopyridine cations was fixed. Because of the negligible interaction of anions Br^- with organic cations, the bromide orbitals were ignored.

Optical Characterization: Temperature-dependent photoluminescence and photoluminescence excitation spectra were measured in the 77–300 K range using the Agilent Cary Eclipse spectrofluorometer. The sample was fixed in a quartz dewar in the cuvette compartment of the spectrofluorometer. Photoluminescence spectra were obtained with 365 nm excitation, and photoluminescence excitation spectra were recorded at 510 nm. The emission slit width was 5 nm, and the excitation slit width was 2.5 nm in both cases.

Powder was prepared by grinding single crystals in an agate mortar. The diffuse reflectance spectra of the powder were obtained using the Cary 5000 UV–vis–NIR spectrometer equipped with a diffuse reflectance accessory DRA 2500. $BaSO_4$ powder was used as the reference material.

Raman Scattering Characterization: Raman scattering measurements were carried out in the temperature range of 83–300 K using the Horiba LabRam HR 800 spectrometer with the grating of 1800 l mm^{-1} and a spectral resolution of 2 cm^{-1}. A solid-state laser with the wavelength of 532 nm and the power of 10 mW was used as an excitation source. The sample was cooled using the Linkam LNP95 system. An Olympus BX41 microscope with the (10×)/0.75 numerical aperture objective lens was used to focus the laser beam on a sample surface.

[CCDC 2065528–2065529 contains the supplementary crystallographic data for this paper. These data can be obtained free of charge from The Cambridge Crystallographic Data Centre via www.ccdc.cam.ac.uk/data_request/cif.]

Supporting Information

Supporting Information is available from the Wiley Online Library or from the author.

Acknowledgements

This study was supported by the Russian Foundation of Basic Research (Project No. 19-03-00836) and by Saint Petersburg State University via a research (Grant ID 73032813). Work at the University of Crete was supported in part by the project "NANO-TANDEM" (MIS 5029191), co-financed by Greece, and the European Regional Development Fund, and in part by SARF UoC under Grant No. KA 10652. This work was carried out on the equipment of SPbU Resource centers "Nanophotonics," "X-Ray Diffraction Studies," "Computer Center," "Physical Methods of Surface Investigation," and "Geomodel."

Open access funding enabled and organized by Projekt DEAL.

Conflict of Interest

The authors declare no conflict of interest.

Data Availability Statement

Data available on request from the authors.

Keywords

halide perovskites, post-perovskites, quantum wells, semiconductors, single crystals

Received: March 9, 2021
Revised: April 26, 2021
Published online: July 3, 2021

[1] H. L. Wells, *Am. J. Sci.* **1893**, *3*, 121.
[2] I. P. Pashuk, N. S. Pidzyrailo, M. G. Matsko, *Sov. Phys. Solid State* **1981**, *23*, 1263.
[3] D. Frohlich, K. Heidrich, H. Kunzel, G. Trendel, J. Treusch, *J. Lumin.* **1979**, *18/19*, 385.
[4] A. Kojima, K. Teshima, Y. Shirai, T. Miyasaka, *J. Am. Chem. Soc.* **2009**, *131*, 6050.
[5] NREL, Best Research-Cell Efficiency Chart, https://www.nrel.gov/pv/cell-efficiency.html (accessed: March 2021).

[6] M. Ahmadi, T. Wu, B. Hu, *Adv. Mater.* **2017**, *29*, 1605242.
[7] Q. V. Le, H. W. Jang, S. Y. Kim, *Small Methods* **2018**, *2*, 1700419.
[8] H. Dong, C. Zhang, X. Liu, J. Yao, Y. Sh. Zhao, *Chem. Soc. Rev.* **2020**, *49*, 951.
[9] H. Wei, J. Huang, *Nat. Commun.* **2019**, *10*, 1066.
[10] V. M. Goldschmidt, *Naturwissenschaften* **1926**, *14*, 477.
[11] O. Y. Khyzhun, P. M. Fochuk, I. V. Kityk, M. Piasecki, S. I. Levkovets, A. O. Fedorchuk, O. V. Parasyuk, *Mater. Chem. Phys.* **2016**, *172*, 165.
[12] C. K. Møller, *Nature* **1958**, *182*, 1436.
[13] L. Mao, C. C. Stoumpos, M. G. Kanatzidis, *J. Am. Chem. Soc.* **2019**, *141*, 1171.
[14] M. D. Smith, B. A. Connor, H. I. Karunadasa, *Chem. Rev.* **2019**, *119*, 3104.
[15] J.-C. Blancon, A. V. Stier, H. Tsai, W. Nie, C. C. Stoumpos, B. Traoré, L. Pedesseau, M. Kepenekian, F. Katsutani, G. T. Noe, J. Kono, S. Tretiak, S. A. Crooker, C. Katan, M. G. Kanatzidis, J. J. Crochet, J. Even, A. D. Mohite, *Nat. Commun.* **2018**, *9*, 2254.
[16] M. Hirasawa, T. Ishihara, T. Goto, *J. Phys. Soc. Jpn.* **1994**, *63*, 3870.
[17] Z. Wang, Q. Lin, F. P. Chmiel, N. Sakai, L. M. Herz, H. J. Snaith, *Nat. Energy* **2017**, *2*, 17135.
[18] A. Krishna, S. Gottis, M. K. Nazeeruddin, F. Sauvage, *Adv. Funct. Mater.* **2019**, *29*, 1806482.
[19] E. P. Booker, M. B. Price, P. J. Budden, H. Abolins, Y. del Valle-Inclan Redondo, L. Eyre, I. Nasrallah, R. T. Phillips, R. H. Friend, F. Deschler, N. C. Greenham, *Adv. Opt. Mater.* **2018**, *6*, 1800616.
[20] E. I. Marchenko, S. A. Fateev, A. A. Petrov, V. V. Korolev, A. Mitrofanov, A. V. Petrov, E. A. Goodilin, A. B. Tarasov, *Chem. Mater.* **2020**, *32*, 7383.
[21] A. R. Oganov, S. Ono, *Nature* **2004**, *430*, 445.
[22] M. Murakami, K. Hirose, K. Kawamura, N. Sata, Y. Ohishi, *Science* **2004**, *304*, 855.
[23] K. Hirose, K. Kawamura, Y. Ohishi, S. Tateno, N. Sata, *Am. Mineral.* **2005**, *90*, 262.
[24] S. Tateno, K. Hirose, N. Sata, Y. Ohishi, *Phys. Chem. Miner.* **2006**, *32*, 721.
[25] K. Hirose, Y. Fujita, *Geophys. Res. Lett.* **2005**, *32*, L13313.
[26] H. Kojitani, Y. Shirako, M. Akaogi, *Phys. Earth Planet. Inter.* **2007**, *165*, 127.
[27] A. Lindsay-Scott, I. G. Wood, D. P. Dobson, L. Vocadlo, J. P. Brodholt, K. S. Knight, M. G. Tucker, T. Taniguchi, *J. Appl. Crystallogr.* **2011**, *44*, 999.
[28] H.-Z. Liu, J. Chen, J. Hu, C. D. Martin, D. J. Weidner, D. Häusermann, H.-K. Mao, *Geophys. Res. Lett.* **2005**, *32*, L04304.
[29] G. B. Jin, E. S. Choi, R. P. Guertin, J. S. Brooks, C. H. Booth, T. E. Albrecht-Schmitt, *Inorg. Chem.* **2007**, *46*, 9213.
[30] G. B. Jin, E. Ringe, G. J. Long, F. Grandjean, M. T. Sougrati, E. S. Choi, D. M. Wells, M. Balasubramanian, J. A. Ibers, *Inorg. Chem.* **2010**, *49*, 10455.
[31] B. Wang, K. Ohgushi, *Sci. Rep.* **2016**, *6*, 37896.
[32] W. Stoeger, *Z. Naturforsch., B: J. Chem. Sci.* **2015**, *32*, 975.
[33] W. Lin, J. He, K. M. McCall, C. C. Stoumpos, Z. Liu, I. Hadar, S. Das, H.-H. Wang, B.-X. Wang, D. Y. Chung, B. W. Wessels, M. G. Kanatzidis, *Adv. Funct. Mater.* **2021**, *31*, 2006635.
[34] R. Gautier, F. Massuyeau, G. Galnon, M. Paris, *Adv. Mater.* **2019**, *31*, 1807383.
[35] R. Kevorkyants, N. I. Selivanov, A. V. Emeline, unpublished.
[36] N. I. Selivanov, A. O. Murzin, V. I. Yudin, Y. V. Kapitonov, A. V. Emeline, arXiv:2104.03175, **2021**.
[37] T. Steiner, *Angew. Chem.* **2002**, *41*, 48.
[38] T. Umebayashi, K. Asai, T. Kondo, A. Nakao, *Phys. Rev. B* **2003**, *67*, 155405.
[39] N. I. Selivanov, Y. A. Rozhkova, R. Kevorkyants, A. V. Emeline, D. W. Bahnemann, *Dalton Trans.* **2020**, *49*, 4390.
[40] O. A. Lozhkina, A. A. Murashkina, V. V. Shilovskikh, Y. V. Kapitonov, V. K. Ryabchuk, A. V. Emeline, T. Miyasaka, *J. Phys. Chem. Lett.* **2018**, *9*, 5408.
[41] P. K. Nayak, M. Sendner, B. Wenger, Z. Wang, K. Sharma, A. J. Ramadan, R. Lovrinčić, A. Pucci, P. K. Madhu, H. J. Snaith, *J. Am. Chem. Soc.* **2018**, *140*, 574.
[42] M. D. Smith, A. Jaffe, E. R. Dohner, A. M. Lindenberg, H. I. Karunadasa, *Chem. Sci.* **2017**, *8*, 4497.
[43] O. A. Lozhkina, V. I. Yudin, A. A. Murashkina, V. V. Shilovskikh, V. G. Davydov, R. Kevorkyants, A. V. Emeline, Y. V. Kapitonov, D. W. Bahnemann, *J. Phys. Chem. Lett.* **2018**, *9*, 302.
[44] Y. Guo, O. Yaffe, D. W. Paley, A. N. Beecher, T. D. Hull, G. Szpak, J. S. Owen, L. E. Brus, M. A. Pimenta, *Phys. Rev. Mater.* **2017**, *1*, 042401.
[45] D. H. Fabini, G. Laurita, J. S. Bechtel, C. C. Stoumpos, H. A. Evans, A. G. Kontos, Y. S. Raptis, P. Falaras, A. Van der Ven, M. G. Kanatzidis, R. Seshadri, *J. Am. Chem. Soc.* **2016**, *138*, 11820.
[46] D. H. Fabini, C. C. Stoumpos, G. Laurita, A. Kaltzoglou, A. G. Kontos, P. Falaras, M. G. Kanatzidis, R. Seshadri, *Angew. Chem.* **2016**, *128*, 15618.
[47] G. Laurita, D. H. Fabini, C. C. Stoumpos, M. G. Kanatzidis, R. Seshadri, *Chem. Sci.* **2017**, *8*, 5628.
[48] V. Petricek, M. Dusek, L. Palatinus, *Z. Kristallogr.* **2014**, *229*, 345.
[49] L. Palatinus, G. Chapuis, *J. Appl. Crystallogr.* **2007**, *40*, 786.
[50] X. Gonze, B. Amadon, P. M. Anglade, J.-M. Beuken, F. Bottin, P. Boulanger, F. Bruneval, D. Caliste, R. Caracas, M. Cote, T. Deutsch, L. Genovese, P. Ghosez, M. Giantomassi, S. Goedecker, D. Hamann, P. Hermet, F. Jollet, G. Jomard, S. Leroux, M. Mancini, S. Mazevet, M. J. T. Oliveira, G. Onida, Y. Pouillon, T. Rangel, G.-M. Rignanese, D. Sangalli, R. Shaltaf, M. Torrent, M. J. Verstraete, G. Zérah, J. W. Zwanziger, *Comput. Phys. Commun.* **2009**, *180*, 2582.
[51] D. M. Ceperley, B. J. Alder, *Phys. Rev. Lett.* **1980**, *45*, 566.
[52] C. Hartwigsen, S. Goedecker, J. Hutter, *Phys. Rev. B* **1998**, *58*, 3641.
[53] H. J. Monkhorst, J. D. Pack, *Phys. Rev. B* **1976**, *13*, 5188.
[54] W. Setyawan, S. Curtarolo, *Comput. Mater. Sci.* **2010**, *49*, 299.